

pubs.acs.org/JACS Article

Facet-Defined Dilute Metal Alloy Nanorods for Efficient Electroreduction of CO₂ to *n*-Propanol

Soojin Jeong,[#] Chuanliang Huang,[#] Zachary Levell,[#] Rebecca X. Skalla, Wei Hong, Nicole J. Escorcia, Yaroslav Losovyj, Baixu Zhu, Alex N. Butrum-Griffith, Yang Liu, Christina W. Li, Danielle Reifsnyder Hickey, Yuanyue Liu,^{*} and Xingchen Ye^{*}



Cite This: https://doi.org/10.1021/jacs.3c11013



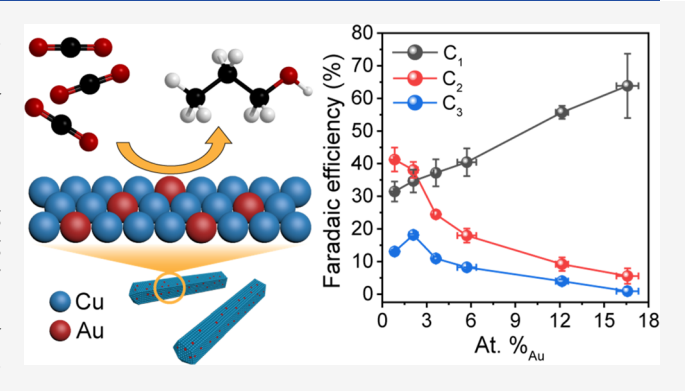
ACCESS

Metrics & More

Article Recommendations

s Supporting Information

ABSTRACT: Electroreduction of CO_2 into liquid fuels is a compelling strategy for storing intermittent renewable energy. Here, we introduce a family of facet-defined dilute copper alloy nanocrystals as catalysts to improve the electrosynthesis of n-propanol from CO_2 and H_2O . We show that substituting a dilute amount of weak-CO-binding metals into the Cu(100) surface improves CO_2 -to-n-propanol activity and selectivity by modifying the electronic structure of catalysts to facilitate C_1 – C_2 coupling while preserving the (100)-like 4-fold Cu ensembles which favor C_1 – C_1 coupling. With the $Au_{0.02}Cu_{0.98}$ champion catalyst, we achieve an n-propanol Faradaic efficiency of $18.2 \pm 0.3\%$ at a low potential of -0.41 V versus the reversible hydrogen electrode and a peak production rate of 16.6 mA·cm $^{-2}$. This study demonstrates



that shape-controlled dilute-metal-alloy nanocrystals represent a new frontier in electrocatalyst design, and precise control of the host and minority metal distributions is crucial for elucidating structure—composition—property relationships and attaining superior catalytic performance.

INTRODUCTION

Electroreduction of CO₂ into value-added chemicals and fuels is a compelling strategy for storing energies derived from intermittent renewable sources while reducing anthropogenic CO₂ emissions.¹⁻⁶ Alcohols are desirable products of the electrochemical CO₂ reduction reaction (CO₂RR) owing to their high energy densities and ease of storage and transportation as liquid fuels. $^{3,7-10}$ Among the C_1-C_3 alcohols, npropanol possesses the highest energy density (27 MJ·L⁻¹) and a high octane number of 118, making its fuel efficiency approach that of gasoline.^{7,11} CO₂RR to *n*-propanol is a kinetically sluggish reaction because it requires the overall transfer of 18 electrons and formation of two C-C bonds (Table S1). Also, the inadequate stabilization of *C₂ intermediates (* denotes surface-adsorbed species) can lead to undesirable C2 product desorption rather than further intermolecular coupling with $*C_1$ to produce C_3 products. $^{12-14}$ The CO₂RR to n-propanol selectivity of existing catalysts has largely remained less than 10%, with few examples exceeding 10% at high overpotentials using H-type electrochemical cells. 15-18 Ču is a unique metal as it can drive C-C bond formation during CO_2RR to generate highly reduced C_{2+} products. $^{1-4,9,15,19-26}$ It has been shown that CO-COdimerization is more favorable on Cu(100) than that on Cu(111), 11,15,27,28 yet the formation of C_3 products is slow on Cu(100) due to the large energy barrier associated with the C_1 – C_2 coupling step. ¹¹ After decades of research, it has been realized that the total intrinsic CO_2RR activity of various monometallic Cu catalysts, being nanostructured or bulk polycrystalline, is very similar after normalization by the electrochemically active surface area (ECSA). ^{4,29} This analysis calls for a critical rethinking of design strategies for a more efficient Cu-based CO_2RR catalyst.

Dilute metal alloys (DMAs) have emerged as a new class of materials with unique properties due to the synergistic combination of metals.³⁰ For heterogeneous catalysis, the addition of foreign metals can modulate the atomic ensembles for adsorbate binding and induce lattice strain and charge transfer that alter the d-band center of the host metal, both of which have been effective in enhancing catalytic activity and selectivity.³⁰ The limit of dilute alloying is single-atom alloy (SAA).³¹ Emergent properties such as free-atom-like states of the dopants were discovered recently in several SAAs, which

Received: October 6, 2023 Revised: January 7, 2024 Accepted: January 9, 2024



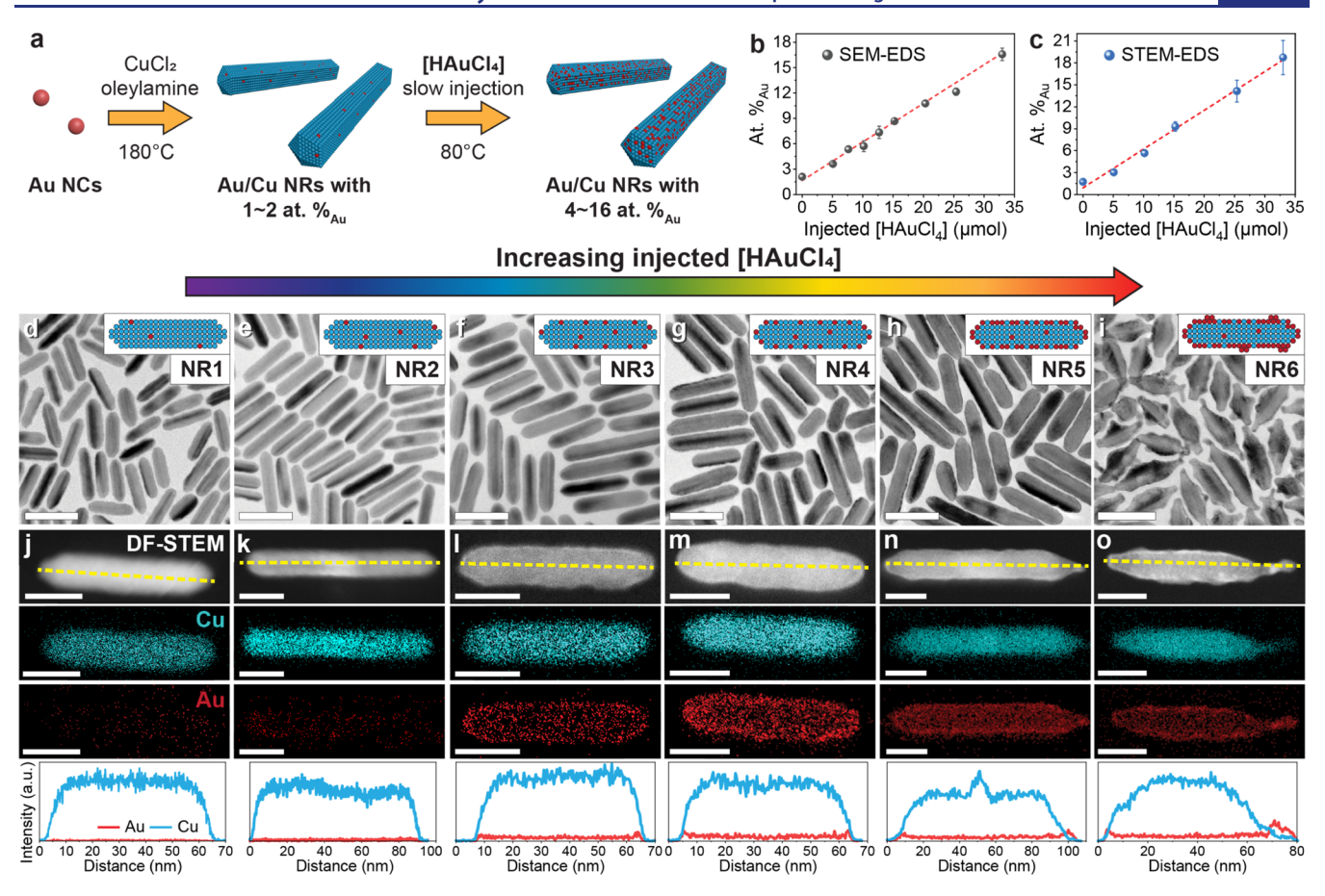


Figure 1. Synthesis and electron microscopy characterization of Au/Cu NRs. (a) Scheme of Au/Cu NR synthesis. (b, c) Elemental analysis results of Au/Cu NRs measured by (b) SEM-EDS and (c) STEM-EDS mapping. (d-i) TEM images of Au/Cu NRs and (j-o) HAADF-STEM image and STEM-EDS elemental maps of a single NR with (d, j) 0.8 ± 0.1 , (e, k) 2.1 ± 0.3 , (f, l) 3.6 ± 0.2 , (g, m) 5.7 ± 0.6 , (h, n) 12.2 ± 0.4 , and (i, o) 16.4 ± 0.7 at. %_{Au}. Inset of (d-i): Schematic depictions of NR microstructures with blue (red) spheres representing Cu (Au) atoms. Bottom of (j-o): STEM-EDS line profiles of Cu and Au along the yellow dashed lines indicated in the corresponding HAADF-STEM images. Scale bars: (d-i) 50 nm and (j-o) 20 nm.

was attributed to the weak wave function mixing between constituent metals.³² This unusual feature promises to break the scaling relationships that limit conventional metal catalysts. For CO₂RR, introducing CO-generating moieties such as Fe(III)-porphyrin complex, ¹⁰ Au, ^{3,33,34} and Zn islands ³⁵ onto the Cu surface has led to enhanced C2+ product formation plausibly by increasing the local concentration of *CO around Cu sites.³⁶ Notably, Jaramillo and co-workers examined a series of Au-on-Cu catalysts made by thermal evaporation of Au onto Cu foils and observed enhanced activities of CO₂RR to ethanol at low Au concentrations.3 Recently, Pb/Cu SAA (4.4 wt % Pb) showed 96% FE for CO₂RR to formate, which was significant given that Pb-free Cu only had 20% formate selectivity.³⁷ These studies motivated us to design and synthesize well-defined Cu-based DMA nanocrystal catalysts to more efficiently and selectively produce energy-dense fuels such as *n*-propanol. We hypothesize that substituting a dilute amount of weak-CO-binding metals (e.g., Au and Ag) into the C₂-favoring Cu(100) surface could improve CO₂RR activity and selectivity toward C₃ products by (i) modifying the electronic structure of Cu(100) to increase local *CO concentration while preserving the (100)-like 4-fold Cu ensembles which favor C_1-C_1 coupling, and (ii) introducing CO-repulsion zones to better co-locate *CO and *C2 intermediates thereby facilitating C_1-C_2 coupling.

Herein, we describe the synthesis of colloidal Au/Cu bimetallic nanorods (NRs) with Au-atom dispersion states tunable from dilute random alloys to continuous ensembles of Au. In contrast to many previous studies of Au/Cu alloy CO_2RR catalysts which comprised more than 20 at. $%_{Au}$ and produced primarily C_1 products (e.g., CO, formate), 2,38 we found that the Faradaic efficiency (FE) of CO₂-to-n-propanol reduction exhibited a volcano-shaped trend with respect to surface Au concentration, reaching a record-high $FE_{n-propanol}$ of $18.2 \pm 0.3\%$ at a modest overpotential of 500 mV (-0.41 V vs the reversible hydrogen electrode (RHE)) with the champion 2 at. %_{Au} DMA catalyst. X-ray photoelectron spectroscopy (XPS), in situ vibrational spectroscopy, and density functional theory (DFT) calculations reveal that low concentrations of Au dopants modify the electronic properties of nearby Cu sites and Au doping lowers the barrier of C1-C2 coupling thus boosting C₃ production during CO₂RR.

■ RESULTS AND DISCUSSION

Synthesis and Structural Characterization of Au/Cu NRs. The atomic percentage of Au for Au/Cu NRs was varied by adjusting the size of Au seeds during heterometallic seeded growth or through overgrowth onto preformed NRs (Figure 1a). Specifically, DMA NRs with less than 3 at. %_{Au} (denoted as NR1 and NR2) were synthesized using 4.4 and 6.5 nm Au

nanocrystals as seeds (Figures S1-S3 and Table S2).³⁹ To prepare NRs with higher Au content, the reaction temperature was lowered from 180 to 80 °C 20 min after injecting Au seeds and a certain amount of Au(III)-OLAM complex was added slowly (50 μ L·min⁻¹) to the reaction solution (Table S2). The rapid surface diffusion of Au on Cu and facile alloying between the two metals likely suppressed the hollowing of the NRs driven by galvanic replacement between Cu⁰ and Au³⁺. Energydispersive X-ray spectroscopy (EDS) analysis of many NRs using a scanning electron microscope (SEM) and scanning transmission electron microscopy (STEM) conducted over a few NRs both indicated that the overall Au content increased gradually from ca. 1 at. % to more than 16 at. % across the sample series NR1-NR6 (Figure 1b,c and Table S2). STEM-EDS Au maps were dominated by scattered dots (NR1 and NR2), discrete clusters (NR3), a semicontinuous surface layer (NR4), and a conformal surface layer (NR5 and NR6) (Figure 1d-o). High-angle annular dark-field STEM (HAADF-STEM) imaging revealed that Au atoms were well dispersed within the Cu matrix for NR1 and NR2 and became increasingly surfaceenriched for NR3-NR6 (Figures 1d-o and S4-S7). All peaks in the powder X-ray diffraction (XRD) patterns of NR1-NR4 can be indexed as face-centered cubic (fcc) Cu (Figure 2a and Tables S3-S4). By contrast, a new set of peaks corresponding to fcc Au was seen for NR5 and NR6 indicating the formation of nanocrystalline Au. Significantly, the Cu(111) diffraction peak exhibited negligible shifts (ca. 0.14°) from NR1 to NR6, which suggests that alloying of Au into the Cu NR interior was

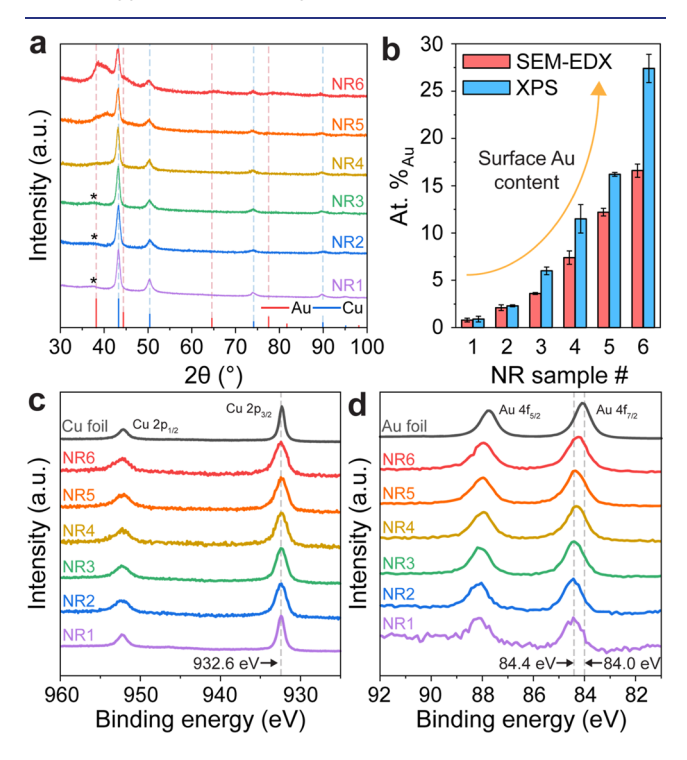


Figure 2. XRD and XPS characterization of Au/Cu NRs. (a) Powder XRD patterns of NRs. The vertical bars at the bottom depict the standard diffraction patterns of Au (JCPDS card no. 00-004-0784) and Cu (JCPDS card no. 00-004-0836). The peak at 37.5° (denoted by asterisks) for NR1, NR2, and NR3 is attributed to Cu2O likely caused by surface oxidation. (b) Comparison of Au percentages of different NRs measured by SEM-EDS (red) and XPS (blue). (c, d) High-resolution XPS spectra in the (c) Cu 2p and (d) Au 4f regions for different NRs.

insignificant for NR3-NR6 and that deposited Au atoms mainly resided on the NR surface.

XPS was used to analyze the surface composition and electronic structure of the Au/Cu NRs. No metal species other than Cu and Au were observed from XPS survey scans (Figure S8). For NR1 and NR2, XPS-derived surface composition closely mirrored that determined by SEM-EDS, indicating a homogeneous distribution of Au atoms within the NRs. On the other hand, XPS-derived Au percentages for NR3-NR6 were appreciably higher than those measured by SEM-EDS, indicative of surface enrichment of gold (Figure 2b). The Cu 2p core levels showed little variation for NR1-NR6 when compared with the binding energies of Cu foil (Figure 2c). By contrast, the Au 4f core levels shifted to lower binding energies from NR1 to NR6 (Figure 2d), with the Au $4f_{7/2}$ binding energy of NR1 deviating the most from that of Au foil (84.4 vs 84.0 eV). Such an increase in binding energy indicates a loss of d electrons at the Au sites upon alloying with Cu. Due to the prominent screening effect exerted by the d electrons, their removal resulted in a positive shift in the 4f binding energy. 40,41 Furthermore, the magnitude of the charge transfer increases as Au becomes more dilute in Cu. According to the charge compensation model, Au withdraws s-p electrons from Cu to achieve a net gain of electrons, as governed by the electronegativity difference between Cu and Au. 40

We conducted X-ray absorption spectroscopy (XAS) measurements to further probe the local atomic environment and electronic structures of different NRs (Figure 3). The Au L₃-edge and Cu K-edge X-ray absorption near-edge structure (XANES) spectra of NRs exhibited edge energies that are essentially identical to that of the reference Au and Cu foils, respectively, confirming that both Au and Cu are in the metallic state (Figure 3a,b, Tables 1 and S5-S6). The white line intensity of the Au L3-edge spectra, which results from the electronic transition between the occupied 2p levels and the partially filled 5d levels, 41 decreased monotonically from NR3 to NR6 (Figure 3b, inset). We attribute this trend to reduced d-electron transfer from Au to Cu as the number of nearest neighbor Cu atoms surrounding individual Au atoms gets smaller. Notably, all NRs displayed a more intense white line than did the Au foil. This indicates a strong ligand effect between Au and Cu, 40 as also supported by the observed Au 4f core-level shifts (Figure 2d). The low signal-to-noise ratio of the Au L₃-edge XANES spectra for NR1 and NR2 was likely caused by the low Au content of these samples (Figure S9). 42 The Cu K-edge extended X-ray absorption fine structure (EXAFS) spectra of NR2-NR6 were dominated by the Cu-Cu scattering path similar to that of the Cu foil (Figures 3c and S10, Table S5). The insensitivity of Cu coordination environment to NR composition is consistent with the picture of Au being present in small amounts (NR1 and NR2) or mainly on the NR surface (NR3-NR6). On the other hand, Au L₃-edge EXAFS spectra featured predominantly Au-Cu coordination at about 2.6 Å for NR2-NR4, with no evidence of a Au-Au scattering path in the spectra suggesting the lack of continuous Au ensembles (Figures 3d and S11, Table S6). 42,43 Au—Au coordination at 2.8 Å was identified for NR5 and NR6, which points toward the presence of Au crystallites. From NR3 to NR6, the Au-Cu coordination number (CN_{Au-Cu}) decreased from 7.5 to 3.9, whereas the total CN of Au $(CN_{Au-Cu} + CN_{Au-Au})$ remained in the range of 7–10 (Figure 3e and Table 1). These data support the formation of bimetallic surface alloys before the emergence of Au crystallites

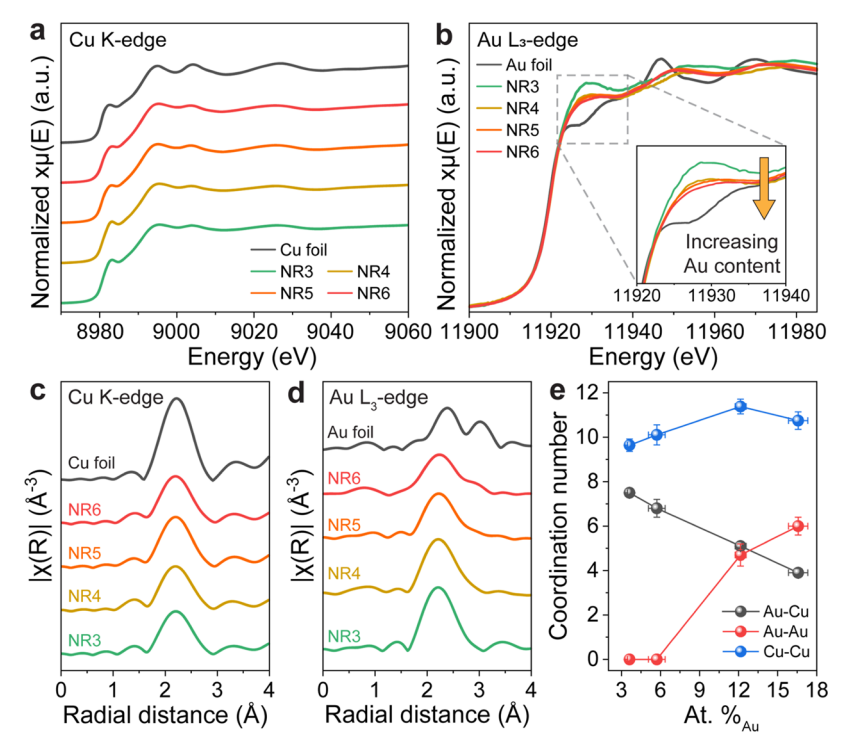


Figure 3. XAS characterization of Au/Cu NRs. (a) Cu K-edge and (b) Au L_3 -edge XANES spectra of different NRs and the Cu or Au foil (black). Inset of (b): An expanded view of the XANES white line region highlighted by dashed box. (c, d) Fourier transform EXAFS spectra for Au/Cu NRs along with the Cu or Au foil (black) at (c) Cu K-edge and (d) Au L_3 -edge. (e) Plots of coordination numbers retrieved from the Au–Cu (black), Au–Au (red), and Cu–Cu (blue) scattering paths versus the Au contents of NRs measured by XPS.

Table 1. Summary of Au L_3 -edge EXAFS Fitting Parameters for Au/Cu NR Samples

sample	edge energy (eV)	scattering path	CN ^a	R (Å)	$\sigma^2 (\mathring{A}^2)^b$	ΔE_0 (eV)
Au foil	11,919.8	Au-Au	12	2.86	0.008	4.9
NR2	11,920.6	Au-Cu	9.7	2.62	0.008	4.8
NR3	11,920.7	Au-Cu	7.5	2.61	0.008	1.4
NR4	11,920.2	Au-Cu	6.8	2.61	0.008	1.7
NR5	11,919.9	Au-Cu	5.1	2.64	0.008	5.3
		Au-Au	4.7	2.83	0.008	
NR6	11,919.4	Au-Cu	3.9	2.63	0.008	4.9
		Au-Au	6.0	2.81	0.008	

"Error bars are provided in Table S6. ${}^b\sigma^2$ was determined through the measurement result of the Au foil and was fixed during EXAFS fittings of different NR samples.

at high Au loadings. Collectively, XPS, XAS, and TEM analysis results establish that NR1-NR3 are shape-controlled DMA nanocrystals with the surface Au concentration tunable from 1 to 6 at. %, whereas NR5-NR6 can be described as bimetallic NRs covered with Au nanocrystallites on the surface.

Electrochemical CO₂RR Performance of Au/Cu NR Catalysts. Constant-current electrolysis was conducted to evaluate the CO₂RR activity and selectivity of different NR catalysts in a 1 M KOH electrolyte. A gas diffusion layer (GDL)-based flow cell was utilized to greatly enhance the reaction rate by improving the mass transport of CO₂ to the cathode (Figures S12–S14). As a benchmark catalyst, polycrystalline Cu film made by thermal evaporation produced similar CO₂RR product distributions as previous reports of similarly prepared samples (Figures 4a and S15), attesting to the reliability of our testing procedures. A range of CO₂RR products including CO, formate, ethylene, ethanol, and *n*-

propanol were detected from different NR catalysts (Figures S16–S17). Compared with the thermally evaporated Cu film, NR2 showed a higher selectivity for C_1 (CO and formate) and C_3 (n-propanol) products and lower selectivity for C_2 products (ethanol and ethylene) at total current densities of 50-200 mA·cm⁻² (Figure 4a). Remarkably, NR2 exhibited a peak FE of $18.2 \pm 0.3\%$ for n-propanol, far exceeding the FE $_n$ -propanol of $4.8 \pm 0.4\%$ for the polycrystalline Cu film.

The library of NR catalysts enables systematic investigation of how the concentration and dispersion states of Au atoms for Au–Cu alloy nanocrystals control the CO₂RR selectivity toward desired C₂₊ products. For all catalysts, the FEs of CO and formate (ethylene and ethanol) decreased (increased) monotonically with increasing current densities (Figure S18). With increasing Au content of the catalyst, C₁ selectivity gradually increased accompanied by a concurrent drop in C₂ selectivity (Figures 4b and S19–S20). Importantly, *n*-propanol selectivity exhibited a volcano-shaped trend reaching the peak FE at 70 mA·cm⁻². This suggests that there is an optimal balance between the coverage of *C₁ and *C₂ intermediates in order to achieve superior C₃ selectivity (Figures 4b,c and S20).

All DMA NRs (NR1-NR3) exhibited enhanced activity for n-propanol production compared to the polycrystalline Cu film (Figure 4d). The n-propanol partial current densities are normalized by the ECSA in order to assess the intrinsic activity of different catalysts (Figures S21–S22 and Table S7). The turnover frequency of n-propanol (TOF $_{n$ -propanol) was estimated based on the number of active sites calculated from ECSA (Figure 4e and Table S8). The predominance of {100} surface planes was supported by the hydroxyl adsorption (OH $_{ads}$) peak position on the cyclic voltammogram (Figure S23) and our previous TEM analysis results. Thus, the lattice constant of the {100} crystal planes was used for TOF calculations.

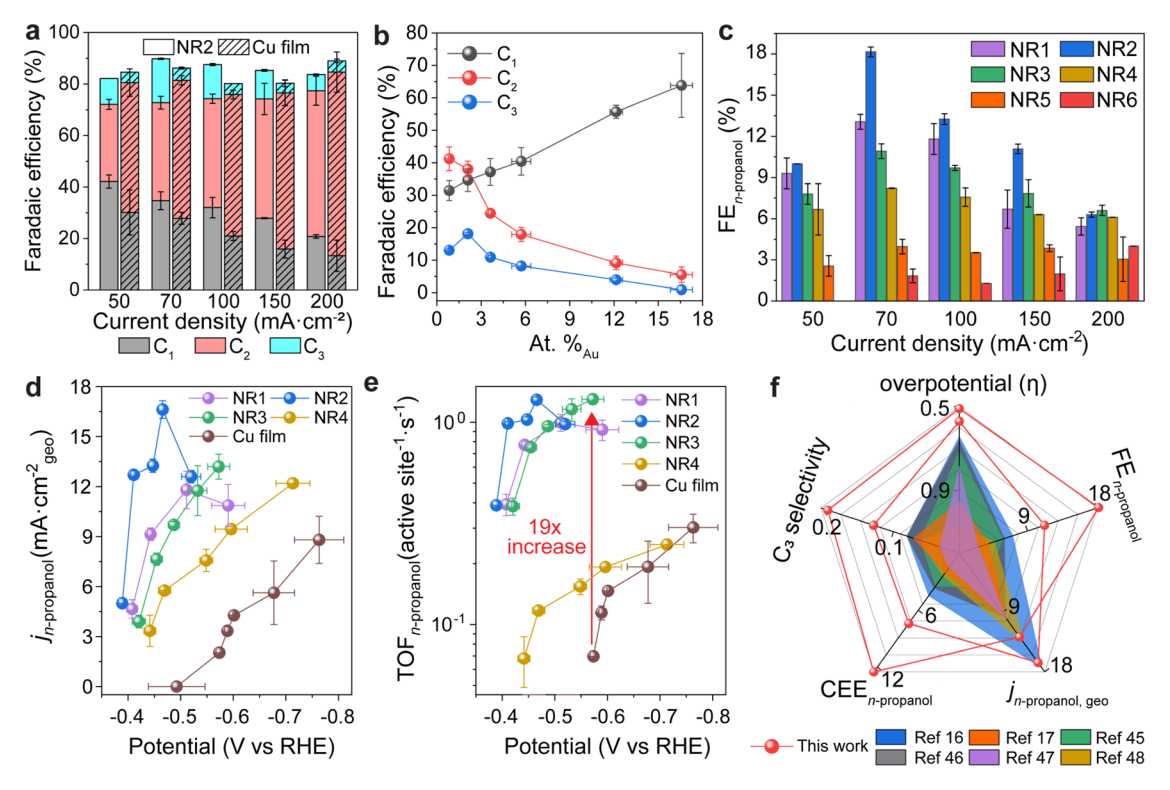


Figure 4. CO₂RR performance of Au/Cu NR catalysts. (a) Comparison of CO₂RR product distributions of NR2 (solid bar) and polycrystalline Cu film (dashed bar) at the total current density of 70 mA·cm⁻² in 1 M KOH electrolyte. (b) Plots of FEs of C₁, C₂, and C₃ products versus the Au contents of NRs measured by SEM-EDS. (c) Summary of *n*-propanol FEs at different applied current densities for different NR catalysts. (d) Partial current densities of *n*-propanol production ($j_{n\text{-propanol}}$) normalized by the geometric area of electrode versus the cathodic potential. (e) Potential-dependent TOF_{*n*-propanol} values obtained by normalizing $j_{n\text{-propanol}}$ to the number of electrochemically active surface sites determined from ECSA. (f) Comparison of CO₂RR performance of NR2 with reported state-of-the-art catalysts evaluated with GDL-based flow cell in terms of overpotential (η), FE, $j_{n\text{-propanol}}$ cathodic energy efficiency for *n*-propanol (CEE_{*n*-propanol}), and C₃ selectivity.

Significantly, NR1-NR3 catalysts exhibited an order-ofmagnitude higher CO₂-to-propanol activity than NR4 or polycrystalline Cu film over a wide potential range (Figure 4e). Long-time electrolysis of the champion NR2 catalyst at 70 mA· cm⁻² showed a stable cell potential of 2.26 ± 0.03 V for 6 h and an average $FE_{ethylene}$, $FE_{ethanol}$, and $FE_{n-propanol}$ of 22.1, 8.0, and 14.1%, respectively (Figure S24a). The decline in FE_{n-propanol} from 18.2 to 10.1% after 6 h most likely results from the accumulation of potassium carbonate on the electrode surface (Figure S24b), which blocks the catalytically active sites for CO₂RR. 44 This argument is also supported by the well-retained morphology and surface composition of the catalyst postelectrolysis suggesting minimal changes in catalyst microstructure (Figure S25). The NR2 catalyst featured a maximum of 18.2 \pm 0.3% FE_{n-propanol} and 16.6 mA·cm_{geo}⁻² for *n*-propanol formation at a moderate cathodic potential of -0.41 V vs RHE. To our knowledge, this is the highest FE_{n-propanol} for electrocatalytic CO₂RR using GDL-based flow cell (Figure S26) and is distinct from previous studies where high selectivity of CO_2RR to *n*-propanol (>10%) was achieved at more negative potentials. ^{16–18} The DMA NR also compares favorably with other catalysts tested with GDL-based flow cells in terms of overpotential (η) , cathodic energy efficiency for npropanol (CEE_{n-propanol}), C₃ product selectivity, and geometric area-normalized current density for n-propanol production $(j_{n-\text{propanol}})$ (Figures 4f and S26, Tables S9-S10). $^{16,17,45-48}$ Besides penta-twinned DMA NRs, single-crystalline Au/Cu DMA nanocubes (2 at. %_{Au}) also showed a high FE_{n-propanol} of 17.0%, whereas pure Cu nanowires and Cu nanocubes

exhibited significantly lower $FE_{n\text{-propanol}}$ (Figure S27). These results indicate that alloying of Cu(100) with dilute Au, rather than Cu(100) surface faceting alone or surface twin boundaries, likely gives rise to superior selectivity toward n-propanol.

Mechanistic Investigations of Enhanced C₃ Selectivity of DMA NR Catalysts. In situ electrochemical attenuated total reflectance surface-enhanced infrared absorption spectroscopy (ATR-SEIRAS) was utilized to probe the adsorption of CO, a key C1 intermediate for n-propanol formation during the CO₂RR (Figures S28-S29). At low overpotentials ranging from -0.04 to -0.17 V, a weak peak at ca. 2040 cm⁻¹ ascribed to top-bound CO was observed. This peak intensified and blue-shifted to ca. 2070 cm⁻¹ as the applied potential became more negative than -0.24 V. This blueshift was plausibly due to a combination of dipole-dipole coupling at high surface coverage of CO and adsorption of CO at undercoordinated defect sites (Figure 5a). 49-51 At -0.65 V, the NR2 catalyst showed a pronounced peak at 2046 cm⁻¹, which can be ascribed to atop-bound CO on Cu(100) (Figure 5b).52 By contrast, a weaker and red-shifted peak (2036 cm⁻¹) was observed for the NR3 catalyst at the same potential (Figure 5c). For CO adsorbed on Cu-based catalysts, it has been shown that weakening of the C-O bond is often concomitant with weakening of the metal-carbon bond due to the pronounced wall effect. 53,54 The wall effect counteracts or even cancels out the effect of strengthening of the metal-CO bond through π back-donation. Therefore, we interpret the observed redshift of the CO stretching frequency from NR2 to

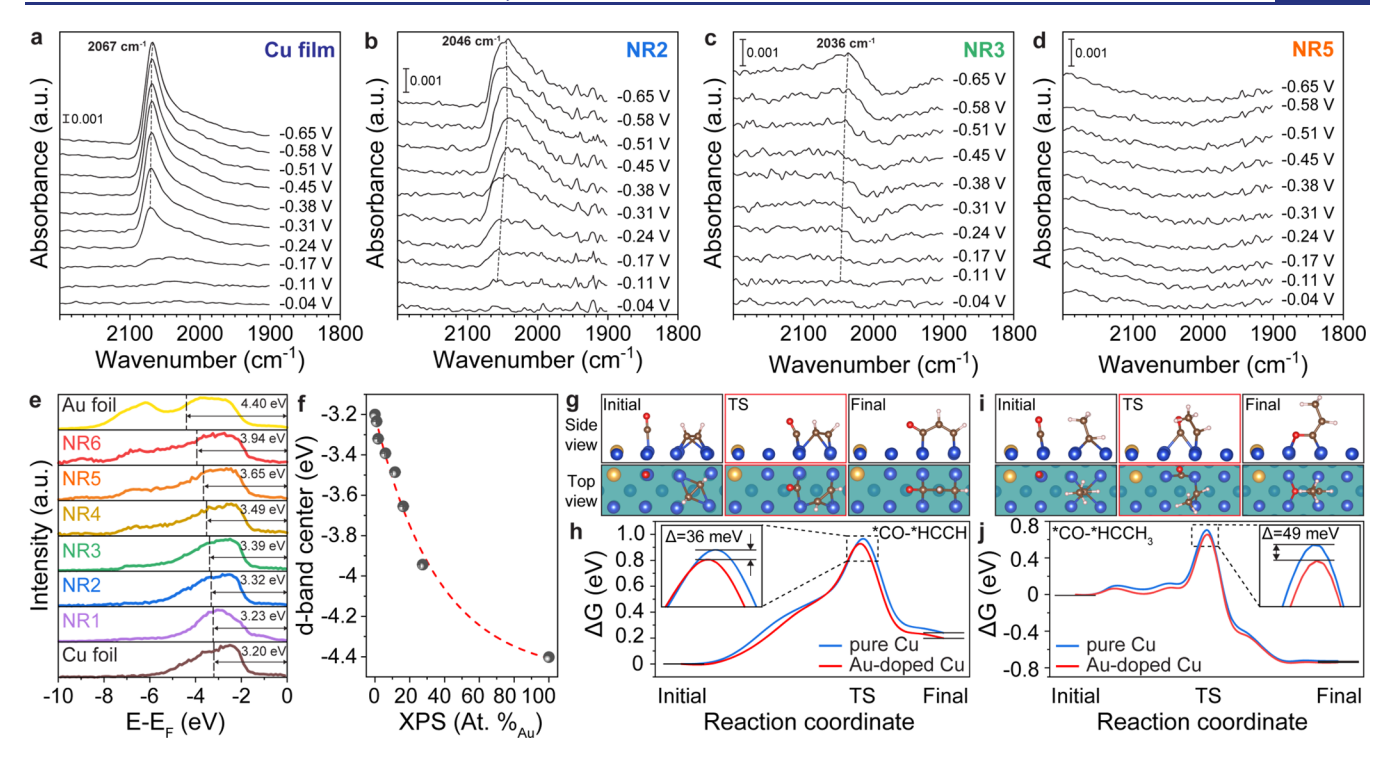


Figure 5. Mechanistic studies of CO₂RR on Au/Cu NR catalysts. (a-d) In situ ATR-SEIRAS spectra recorded at different cathodic potentials for (a) polycrystalline Cu film, (b) NR2, (c) NR3, and (d) NR5 catalysts. (e) XPS valence-band photoemission spectra of Au/Cu NRs, Au foil, and Cu foil. The black dashed lines indicate the d-band centers of different samples. (f) Plot of measured d-band center versus the Au contents of NRs measured by XPS. (g) Top view and side view of the key reaction intermediates for the *CO-*HCCH coupling over pristine and Au-doped Cu(100) surfaces and (h) the corresponding free energy diagrams. (i) Top-view and side-view pictures of the key reaction intermediates for the *CO-*HCCH₃ coupling over pristine and Au-doped Cu(100) surfaces and (j) the corresponding free energy diagrams. The Cu, Au, C, O, and H atoms are represented by blue, yellow, brown, red, and white spheres, respectively.

NR3 as an indication of weakened binding of CO to the metal substrate. The CO peak gradually red-shifted as the working electrode was scanned cathodically, which can be attributed to the vibrational Stark effect with a Stark tuning rate of 36 and 39 cm⁻¹·V⁻¹ for NR2 and NR3, respectively.⁵¹ These values are in line with previous studies on polycrystalline Cu surfaces in alkaline electrolytes.⁵¹ Moreover, NR5 and NR6 did not show any peak related to adsorbed CO species in the same potential range, which is similar to that of polycrystalline Au film and reflects their much weaker binding to CO (Figures 5d and S30). The diminishing CO coverage from NR2 to NR6 was also supported by the valence-band XPS spectra. The surface d-band center gradually shifted away from the Fermi level with increasing Au concentration weakening the binding of catalyst to CO (Figure 5e,f).^{2,38} Consequently, the catalytic activity for CO production increased at higher surface Au content (Figure S18b). Altogether, these results suggest that the NR2 catalyst was able to maintain a high CO coverage during the CO_2RR while not compromising the facile C_1-C_1 coupling of the Cu(100) surface, a key requirement for achieving efficient C_1 – C_2 coupling.

To further elucidate the effects of Au doping in the Cu(100)surface on the energetics of the C_1-C_2 coupling process, we performed DFT calculations using *CO as the C₁ intermediate and *HCCH or *HCCH₃ as the C₂ intermediate (Figure 5gj). At present, the reaction pathways of CO₂RR to n-propanol and the nature of rate-determining C_2 intermediate are still debated in the literature. 8,12,14,55 A recent DFT study of CO₂RR found that the difference in the kinetic barrier between C₁-C₂ coupling and further reduction of the C₂ intermediate

is the smallest for *HCCH, suggesting that it is the most likely C₂ intermediate for *n*-propanol formation.¹⁴ Also, Hori et al. proposed *HCCH₃ as a possible C₂ intermediate for C₁-C₂ coupling during CO₂RR. 55 Therefore, we examined the free energy landscapes of these two coupling reactions. Our DFT calculations reveal that Au doping lowers the energy barriers of *CO-*HCCH (Figure 5g,h) and *CO-*HCCH₃ (Figure 5i,j) couplings by 36 and 49 meV, respectively. These values translate to increased reaction rate constants of n-propanol formation by 4.1 and 6.7 times according to the Arrhenius equation at 298 K. Accordingly, Au substitution enhances C₁-C₂ coupling on Cu(100), and the coupling between *CO and *HCCH₃ is likely the more favorable C_1 – C_2 coupling step for the Au-doped Cu(100) surface than *CO-*HCCH coupling. Other factors such as the dependence of C_1-C_1 and C_1-C_2 couplings on the coverage of various C_1 and C_2 intermediates could also play an important role in dictating the CO₂RR product distributions, which are beyond the scope of this study.

CONCLUSIONS

In summary, we synthesized a library of Au/Cu bimetallic NR catalysts with tunable surface composition by adjusting the size of Au seeds during heterometallic seeded growth or through overgrowth onto preformed NRs. The FEs of C_1 (C_2) products monotonically increased (decreased) with increasing surface Au concentration, suggesting that the coverage of C₁ and C₂ intermediates during the CO2RR depends sensitively on the dispersion and concentration of surface Au dopants in the dilute-alloy regime. Different from previous studies of Au/Cu

alloy CO₂RR catalysts which comprised more than 20 at. %_{Au} and produced primarily C₁ products (e.g., CO, formate), we found that the FE_{n-propanol} exhibited a volcano-shaped trend with respect to surface Au concentration. The champion DMA NR catalyst delivered a record-high FE_{n-propanol} of 18.2 \pm 0.3% and n-propanol partial current density of 16.6 mA·cm_{geo}⁻² at low overpotentials. XPS and in situ FTIR analyses together with DFT calculations indicate that Au doping in the Cu(100) surface modifies the electronic properties of nearby Cu sites and lowers the barrier of C1-C2 coupling enhancing C3 selectivity for CO₂RR. This study demonstrates that facetdefined DMA nanocrystals represent a new frontier in electrocatalyst design and that meticulous control of the concentration and distribution of the minority metals is crucial for elucidating structure-composition-property relationships and for attaining superior catalytic performance.

■ EXPERIMENTAL SECTION

Synthesis of Au Nanocrystal Seeds. Au seeds were synthesized utilizing established methods.³⁹ To prepare 6.5 nm Au seeds, 10 mL of oleylamine (OLAM-TCI, TCI America) was loaded into a 50 mL three-neck round-bottom flask and vacuum-degassed for 30 min. After refilling with N₂, 10 mL of anhydrous toluene and 0.25 mmol (98 mg) of HAuCl₄·3H₂O were added. After the flask was cooled to 20 °C with an ice bath, a mixture consisting of 0.25 mmol (22 mg) borane tert-butylamine complex, 1 mL of OLAM-TCI, and 1 mL of anhydrous toluene was swiftly added to the reaction under stirring. After reacting at 20 °C for 1 h, the resultant nanocrystals were isolated by precipitation with 60 mL of acetone and centrifugation at 6000 rpm for 5 min. The pellet was redispersed in toluene to reach an optical density (O.D.) of 40 at 525.3 nm (plasmonic peak wavelength). The same procedure was used to prepare 4.4 and 9.0 nm Au seeds, except that the reaction was conducted at 25 and 15 °C, respectively.

Synthesis of Au/Cu NRs with 1 at. %_{Au} (NR1) and 2 at. %_{Au} (NR2). NR1 and NR2 were synthesized following our previous report.³⁹ In a typical synthesis of NR1, 0.5 mmol (85 mg) of CuCl₂· 2H₂O and 10 mL of oleylamine (OLAM-SA, Sigma-Aldrich) were loaded into a 50 mL three-neck round-bottom flask. The flask was subjected to three cycles of vacuum degassing at 25 °C followed by N₂ purging to eliminate any oxygen. Next, the mixture was heated at 80 °C to fully dissolve CuCl₂, yielding a blue-colored solution. Afterward, the reaction temperature was raised to 180 °C and 0.1 mL of 4.4 nm Au nanocrystal seed solution (O.D. = 40) was injected under stirring. The reaction mixture was cooled to room temperature after 1 h and the NRs were purified by precipitation with 30 mL of isopropanol and centrifugation at 1500 rpm for 3 min. The pellet was redispersed in anhydrous toluene and stored inside a N2-filled glovebox. To synthesize NR2, the same procedure was employed except that 0.15 mL of 6.5 nm Au seed solution (O.D. = 40) was used.

Synthesis of Au/Cu NRs with 4 at. $\%_{Au}$ (NR3), 6 at. $\%_{Au}$ (NR4), 12 at. Au (NR5), and 16 at. $\%_{Au}$ (NR6). NR3-NR6 were synthesized by introducing extra Au precursors during the typical synthesis of 2 at. % Au/Cu NRs. Specifically, 0.15 mL of 6.5 nm Au nanocrystal seed solution (O.D. = 40) was injected into the mixture of 0.5 mmol CuCl₂·2H₂O and 10 mL of OLAM-SA at 180 °C under N₂ flow. After reacting at 180 °C for 20 min, the temperature was lowered to 80 °C and another precursor solution prepared by dissolving a certain amount of HAuCl₄·3H₂O in 1 mL of OLAM-SA (Table S2) was added at the rate of 50 μ L·min⁻¹ with a syringe pump. Afterward, the reaction mixture was kept at 80 °C for another 10 min before being cooled to room temperature. The NR products were purified via precipitation with 30 mL of isopropanol and centrifugation at 3000 rpm for 3 min. The pellet was redispersed in anhydrous toluene and stored inside a N₂-filled glovebox.

Synthesis of Au/Cu DMA Nanocubes. CuBr₂ (0.5 mmol) and OLAM-SA (10 mL) were added into a 50 mL three-neck round-bottom flask. The flask was then vacuum-degassed and refilled with

 N_2 three times to remove any oxygen. This mixture was kept at room temperature with stirring for 1 h to fully dissolve CuBr₂. Next, 3.6 mmol of anhydrous hydrazine was swiftly added under stirring. After 5 min, 0.20 mL of 9.0 nm Au nanocrystal seed solution (O.D. = 40) was added and the solution was stirred at room temperature for another 15 min. Afterward, the reaction mixture was heated to 180 °C at the ramp rate of 20 °C·min⁻¹. After reacting at 180 °C for 1 h, the solution was cooled to room temperature and the nanocubes were purified by precipitation with 30 mL of isopropanol and centrifugation at 4500 rpm for 3 min. The pellet was redispersed in anhydrous toluene and stored inside a N_2 -filled glovebox.

Synthesis of Cu Nanowires. Cu nanowires were synthesized using established methods. ⁵⁶ Specifically, 1 mmol of CuCl and 3 mL of OLAM-SA were added to a 25 mL three-neck flask, which was N_2 -purged for 15 min under stirring at room temperature. The resultant mixture was then heated to 120 °C and kept at this temperature for 30 min. Afterward, the stirring was stopped, and the solution was rapidly heated to 180 °C. The reaction was allowed to proceed at 180 °C for 90 min before being cooled down to room temperature. The crude products were purified through three cycles of dispersion in anhydrous hexane followed by centrifugation at 1000 rpm for 3 min inside a N_2 -filled glovebox. Finally, the Cu nanowires were redispersed in anhydrous toluene and stored inside a N_2 -filled glovebox.

Synthesis of Cu Nanocubes. Cu nanocubes were synthesized following previously reported methods. ⁵⁷ Specifically, 3 mmol of CuBr, 25 mmol of tri-n-octylphosphine oxide, and 10 mL of OLAM-SA were loaded into a 50 mL three-neck flask, and the resultant mixture was vacuumed and degassed at 100 °C for 1 h. After refilling with N_2 , the reaction solution was quickly heated to 210 °C and was kept at this temperature for 1 h before being cooled down to room temperature. The nanocubes were purified by precipitation with anhydrous 2-propanol and centrifugation at 4500 rpm for 3 min inside a N_2 -filled glovebox. Finally, Cu nanocubes were redispersed in anhydrous toluene and stored in a N_2 -filled glovebox.

Characterization. TEM images were recorded on a JEOL JEM 1400 plus microscope, which was equipped with a LaB₆ filament operating at 120 kV. HAADF-STEM and STEM energy-dispersive Xray spectroscopy (STEM-EDS) analyses were conducted on a 300 kV IEOL IEM 3200FS TEM. Aberration-corrected HAADF-STEM imaging was performed on a 300 kV FEI Titan³ G2 S/TEM, with a probe convergence angle of 25 mrad, a probe current of 0.1 nA, and ADF detector angles of 51 and 300 mrad. Samples for TEM analyses were prepared by drop-casting $\sim 10 \ \mu L$ of a nanocrystal solution onto a 300-mesh carbon-coated nickel grid. Before HAADF-STEM imaging, the specimen underwent 30 min of beam showering in TEM mode with a beam current of 5 nA to minimize carbon contamination. Powder XRD patterns were recorded on a PANalytical Empyrean X-ray diffractometer operating at 40 kV and 35 mA. XRD samples were prepared by drop-casting nanocrystal solutions onto low-background Si substrates.

XPS analyses were conducted on a PHI 5000 VersaProbe II instrument that was equipped with a focused monochromatic Al K α source. The instrument base pressure was about 8 \times 10^{-10} Torr. A beam size of about 100 μm and an X-ray power of 25 W at 15 keV were used. The instrument work function was calibrated to yield a binding energy of 84.0 eV for the $4f_{7/2}$ line of metallic gold. The spectrometer dispersion was adjusted to give binding energies of 284.8 368.3, and 932.7 eV for the C 1s line of adventitious carbon, Ag 3d_{5/2}, and Cu 2p_{3/2} photoemission lines, respectively. Survey spectra were taken with a step size of 0.4 eV and a pass energy of 187.85 eV. High-resolution Au 4f, Cu 2p, and C 1s spectra were recorded with a step size of 0.1 eV and a pass energy of 23.5 eV. All XPS data were acquired using the software SmartSoft-XPS v2.6.3.4 and processed using PHI MultiPak v9.3.0.3 or CasaXPS v.2.3.14 with Shirley background. The relative sensitivity factors from the MultiPak library were used when calculating atomic percentages. To calibrate the binding energy scale, a piece of freshly exfoliated highly oriented pyrolytic graphite (HOPG) was used as the internal standard. The C 1s photoemission line from the surface of HOPG was measured simultaneously with nanocrystal samples in multipoint analysis mode.

Consequently, all XPS spectra were calibrated according to the C 1s peak of HOPG at 284.4 eV. 58

XAS measurements were performed at beamline 10-BM of Advanced Photon Source (Argonne National Laboratory) at the Cu K-edge (8978.9 eV) and Au L₃-edge (11,918.7 eV) in transmission mode. XAS samples were prepared inside of a N2-filled glovebox. Typically, 5 mL of Au/Cu NR solution (10 mg⋅mL⁻¹ in anhydrous toluene) was mixed with 5 mL of carbon black solution (Vulcan XC-72R, 10 mg·mL⁻¹ in anhydrous toluene), and the resultant mixture was stirred overnight before precipitation via centrifugation at 1500 rpm for 3 min. After drying under flowing N2 gas, the pellets were mixed with additional Vulcan XC-72R carbon black powder to attain a gold mass concentration of 2 wt $\%_{\text{Au}}$ before being ground into a fine powder. Afterward, the sample was pressed to form a self-supported wafer, which was placed and sealed inside a gastight sample holder. All XAS measurements were conducted at about 22 °C. During each measurement at a particular edge, the corresponding metal foil was measured simultaneously through a third ion chamber for energy calibration. Analysis and fitting of XAS data were performed using the Demeter software. 59 The XAS spectra of Au foil were fitted based on the standard Au face-centered cubic structure to obtain an amplitude reduction factor (S₀²), which remained fixed during subsequent fittings of the Au L₃-edge data. The same process was applied for the Cu foil, and measurement results at the Cu K-edge. EXAFS coordination parameters were retrieved by least-squares fit in Rspace of the k^2 -weighed Fourier transform data from 3 to 10 Å⁻¹. Fittings of EXAFS data were done by refining the bond distance (R), coordination number (CN), and energy shift (ΔE_0) considering only the first coordination shell. The Debye-Waller factor (σ^2) was fixed

Electrochemical CO₂ Reduction Experiments. All electrochemical measurements were performed on an SP-300 potentiostat (Biologic). CO2 electrolysis was done by using a custom-built gasdiffusion-layer (GDL)-based flow cell with the cathode and anode compartments separated by a piece of Selemion anion-exchange membrane (Figure S12). The flow rate of CO2 gas was regulated using a mass flow controller (Alicat Scientific), and the gas flow rate existing in the cathode compartment was monitored during electrolysis with a mass flow meter (Alicat Scientific) to ensure a gastight setup (Figure S13). The uncompensated resistance (R_n) was determined by using electrochemical impedance spectroscopy (Figure S14). The catholyte and anolyte flow rates were controlled independently by using two peristaltic pumps in a closed-loop configuration. During electrolysis, CO2 gas was flowing continuously at 20 sccm, while the catholyte (10 mL) and the anolyte (10 mL) were circulated at 7.0 and 15.0 mL·min⁻¹, respectively. 1 M KOH solution was used as electrolyte and a leak-free Ag/AgCl electrode (Innovative Instruments, Inc.) was used as the reference electrode.

Unless stated otherwise, the electrochemical potentials have been converted to the RHE scale via $E(vs \, RHE) = E(vs \, Ag/AgCl) + 0.21 \, V + 0.059 \times pH$. The reference electrode was calibrated prior to each electrolysis run by measuring its open-circuit potential against a master Ag/AgCl reference electrode (3 M NaCl, BASi) in 0.1 M HClO₄ solution. The master reference electrode was further calibrated by measuring its open-circuit potential against a Pt foil (99.997%, Alfa Aesar) in H₂-saturated 0.1 M HClO₄ (pH 1.0), which was 0.270 V, or equivalently, 0.210 V vs the standard hydrogen electrode. This master reference electrode was not utilized in other electrochemical experiments.

To prepare the working electrode, a catalyst ink was made by mixing 1 mL of 5 mg·mL⁻¹ NR solution (in anhydrous toluene), 200 μ L of DMSO, 200 μ L of isopropanol, and 50 μ L of 5 wt % Nafion perfluorinated resin solution, followed by sonication for 5 min. Next, 290 μ L of the catalyst ink was drop-cast onto a carbon paper (2 cm × 2 cm, Freudenberg H14C9, Fuel cell store) which was vacuum-dried at room temperature for 2 h. The copper thin-film electrode was prepared by thermal evaporation of copper (Cu shot, 99.999%, Alfa Aesar) at a base pressure of <10⁻⁶ Torr onto a polytetrafluoroethylene (PTFE, Steriltech) GDL with a mean pore size of 200 nm. A deposition rate of 0.067 nm·min⁻¹ was used, which was regulated by

an SQC-310 controller (INFICON). A piece of Ni foam (0.5 cm \times 1 cm x 1.6 mm, Advanced 2D Materials CO., Ltd., Store) was used as the counter electrode.

To quantify the gaseous products generated during the CO_2RR , the cathode compartment was connected to a gas chromatograph (GC, Multiple gas analyzer #5, SRI Instruments) using Ar (99.999%, Airgas) as the carrier gas. The concentrations of CO and C_2H_4 were measured using a flame ionization detector and H_2 was quantified with a thermal conductivity detector. The Faradaic efficiency (FE) of each CO_2RR product was calculated as follows:

$$FE = \frac{C \times \frac{nPV}{RT} \times 96485}{I \times \frac{V}{(f/60)}} \times 100(\%)$$
(1)

where C is the concentration (in ppm) of a specific gaseous product, n is the number of electrons required to form that product (Table S1), P is 1 atm, V is the injection volume (1 mL) of each GC run, R is 0.0821 atm·L·mol⁻¹·K⁻¹, T is 298 K, I is the applied current during electrolysis, and f (in sccm) is the CO₂ flow rate during CO₂RR.

Liquid-phase CO₂RR products were quantified with a 600 MHz Inova NMR spectrometer utilizing a presaturation pulse sequence for water suppression. Typically, 600 μ L of the postelectrolysis electrolyte, 70 μ L of D₂O, and 30 μ L of the internal standard solution (10 mM DMSO and 50 mM phenol in H₂O) were mixed in an NMR sample tube. The amount of formate was quantified by comparing the peak areas of formate (singlet, δ = 8.33 ppm) and phenol (triplet, δ = 7.03 ppm). Other liquid products including ethanol (triplet, δ = 1.06 ppm), acetate (singlet, δ = 1.8 ppm), and n-propanol (triplet, δ = 0.77 ppm) were quantified by comparing their peak areas with that of DMSO (singlet, δ = 2.6 ppm). The calibration curves of individual liquid products were constructed by measuring a series of standard samples with known concentrations (Figure S16). FE was calculated as follows:

$$FE = \frac{n \times 96485 \times C \times V}{I \times t} \times 100(\%)$$
 (2)

where C is the concentration of a certain liquid product determined by NMR, n is the number of electrons required to form that product (Table S1), V is the total volume of catholyte (10 mL), I is the applied current during electrolysis, and t is the duration of the CO_2RR electrolysis before sampling of liquid products.

The energy efficiency of the electrochemical system was calculated as follows: 10

Energy efficiency =
$$\frac{E_{\rm ox}^{0} - E_{\rm red}^{0}}{E_{\rm ox} - E_{\rm red}} \times FE_{n\text{-propanol}}(\%)$$
(3)

where $E_{\rm ox}^0$ and $E_{\rm red}^0$ are the standard equilibrium potentials for water oxidation (1.23 V vs RHE) and CO₂RR to *n*-propanol (0.10 V vs RHE), respectively, and $E_{\rm ox}$ and $E_{\rm red}$ are the applied potentials at the anode and cathode, respectively. To calculate the cathodic energy efficiency, the anodic reaction was assumed to occur with zero overpotential ($E_{\rm ox}=1.23$ V vs RHE).

The long-term stability of CO_2RR catalysts was studied using chronopotentiometry at the current density of 70 mA·cm⁻². A 30 mL portion of 1 M KOH catholyte was used for CO_2RR electrolysis, and 1 mL of catholyte was extracted periodically with a syringe for quantification of liquid products. After 6 h of electrolysis, the pH of the catholyte was found to slightly decrease from 14 to 13.65.

Determination of Electrochemically Active Surface Area (ECSA). The catalyst ECSA was determined from measurements of the double-layer capacitance ($C_{\rm cll}$). Cyclic voltammetry (CV) was performed in CO₂-saturated 0.1 M KHCO₃ in a custom-built H-type cell at various scan rates (80, 100, 120, 140, 160, and 180 mV·s⁻¹) in a potential range where faradaic processes are negligible. CV scans of the reference Cu foil were conducted between 0.16 and 0.20 V, whereas CV scans of all other samples were acquired between 0.40 and 0.50 V (Figure S21 and Table S7). 1,60 The average charging current density ($|j_a - j_c|/2$), defined as half of the difference between anodic (j_a) and cathodic (j_c) current densities at 0.18 (for Cu foil)

and 0.45 V (for all other samples), was plotted versus the scan rate and $C_{\rm dl}$ was given by the slope. ECSA can be calculated as follows:

$$ECSA = A_{geo} \times RF \tag{4}$$

where $A_{\rm geo}$ is the geometric surface area of the electrode (0.5 cm²) and RF is the roughness factor determined as the ratio of catalyst's $C_{\rm dl}$ to $C_{\rm dl}$ of the reference Cu foil (34.9 $\mu{\rm F\cdot cm^{-2}}$) (Table S7). The reference Cu foil electrode was prepared as follows: a piece of Cu foil (1 cm², 99.999%, Alfa Aesar) was mechanically polished with sandpaper (400G, 3M) followed by sonication in a 1:1 (v/v) mixture of DI water and isopropyl alcohol for 5 min. Next, the Cu foil was electropolished by holding it at 2.1 V relative to a graphite foil CE (4 cm², 0.13 mm thick, 99.8%, Alfa Aesar) in 85 wt % phosphoric acid for 5 min in an undivided cell. To prepare the counter electrode for ECSA measurements, a mixture of 252 $\mu{\rm L}$ of isopropanol, 252 $\mu{\rm L}$ of DI water, 20 $\mu{\rm L}$ of Nafion solution, and 6 mg of iridium(IV) oxide (99%, Alfa Aesar) was sonicated for 20 min to achieve a homogeneous ink. 52.4 $\mu{\rm L}$ of this ink was then drop-cast onto a carbon paper (1 cm², Toray-060, Fuel Cell Store) and dried under vacuum.

Calculation of the Number of Electrochemically Active Surface Atoms. The number of electrochemically active surface atoms was calculated using the lattice constant of the Au–Cu alloy and experimentally determined ECSA. The results are summarized in Table S8. The lattice constant of a bimetallic Au–Cu surface alloy was estimated based on Vegard's law using the atomic percentages measured by XPS. Only NR1-NR4 catalysts with minimal presence of continuous gold domains (based on XAS data) were analyzed, given that Vegard's law is applicable to substitutional solid solutions with randomly distributed atoms. The surface lattice constant of NR catalysts ($a_{\rm NR}$) was calculated as follows:

$$a_{\rm NR} = (1 - x)a_{\rm Cu} + xa_{\rm Au} \tag{5}$$

where x is the atomic percentage of gold measured by XPS, $a_{\rm Cu}$ is the lattice constant of bulk Cu (0.362 nm), and $a_{\rm Au}$ is the lattice constant of bulk Au (0.408 nm). Our electron microscopy³⁹ and electrochemical CV characterization indicate that the NR surface is terminated predominantly by {100} crystal planes (Figure S23). Here, CV was conducted in Ar-purged 1 M KOH (aqueous) at 50 mV·s⁻¹ using a custom-built H-type cell and IrO₂-deposited carbon paper as the counter electrode. Previous studies have shown that OH adsorption on Cu is a structure-sensitive process. Gi Given that each surface unit cell of the Cu {100} planes consists of two atoms, the total number of surface Au and Cu atoms can be calculated as $2 \times \frac{\rm ECSA(cm^2)}{(a_{\rm NR})^2 {\rm cm}^2}$

Turnover Frequency Calculation. The turnover frequency of n-propanol ($TOF_{n\text{-propanol}}$) was calculated as the number of n-propanol molecules produced per second per surface active site as follows:

$$TOF_{n-propanol} = \frac{I \times N_{A} \times FE_{n-propanol}}{F \times 18 \times N_{active}}$$
(6)

where I is the current during electrolysis, N_A is the Avogadro constant, ${\rm FE}_{n\text{-propanol}}$ is the Faraday efficiency of n-propanol, F is the Faraday constant, and $N_{\rm active}$ is the number of surface active sites. The factor "18" accounts for the fact that the formation of one n-propanol molecule requires 18 electrons.

In Situ ATR-SEIRAS. ATR-SEIRAS was performed on a Bruker Vertex 70v FTIR spectrometer, which was equipped with a liquid nitrogen-cooled MCT detector and a VeeMAX III ATR accessory (Pike Technologies). A custom-built spectro-electrochemical cell was used, with the anode and cathode compartments separated by a Selemion anion-exchange membrane (Figure S28a). A thin film of polycrystalline Au, polycrystalline Cu, or NR catalysts was deposited onto the reflecting surface of a Si ATR crystal with a 60° incidence angle (Pike Technologies), which served as the working electrode. A graphite rod (99.9995%, Alfa Aesar) was employed as the counter electrode, and Ag/AgCl (3 M NaCl, BASi) was used as the reference electrode. All measurements were conducted in a 0.1 M KOH

electrolyte. The catholyte was purged with CO gas for 15 min before the ATR-SEIRAS measurement and was continuously purged with CO throughout the measurement. To minimize any potential drift, the Ag/AgCl reference electrode was installed immediately before the measurement to limit its contact with the KOH electrolyte to less than 5 min. All spectra were collected at 4 cm $^{-1}$ resolution with 0.85 s per scan. As a result, a spectrum of 8 (128) coadded scans corresponds to 6.8 s (108.8 s).

In a typical ATR-SEIRAS experiment, a background spectrum was first obtained with 128 coadded scans while holding the potential at 0.03 V using a potentiostat (Wavedriver 200, PINE research). Next, CV was conducted at 10 $\rm mV\cdot s^{-1}$ between 0.03 V and -0.67 V. Individual spectra were collected with 8 coadded scans and thus, each spectrum corresponded to about 68 mV potential interval (Figures S29–S30). The spectra are presented in absorbance units, where positive peaks indicate an increase in the concentration of relevant interfacial species.

Preparation of Gold Film. Polycrystalline gold film was prepared on the reflecting plane of the Si ATR crystal using electroless deposition following established methods.⁶² First, the surface of the Si prism was cleaned by dipping it into aqua regia for 2 min to dissolve any metal contaminants and then rinsed with copious amounts of DI water. Afterward, the Si prism surface was mechanically polished with a suspension of 0.05 μ m alumina powder in DI water and then sonicated in DI water for 5 min to remove any residual alumina powders. Next, the polished Si surface was immersed in freshly prepared Piranha solution (3:1 v/v ratio of H₂SO₄:H₂O₂) for 20 min to remove any organic contaminants. The Si prism was then sonicated in water, acetone, and water successively, each for 5 min, resulting in a highly hydrophilic surface. The cleaned Si prism surface was immersed in a 40% NH₄F solution for 90 s at room temperature to create a hydrogen-terminated Si surface. The hydrophilicity (hydrophobicity) of the Si surface was judged by the tendency of a water droplet to wet the surface (bead at the surface). Separately, a 2 wt % HF solution was added to the gold plating bath (1:4.4 v/v ratio) at 55 °C. After 30 s, the hydrogen-terminated Si surface was immersed in the gold plating bath at 55 °C for 8 min, rinsed with DI water, and blown dry with N2 gas.

The gold plating bath was prepared by mixing two solutions (solutions A and B) as follows. To prepare *solution A*, 0.1143 g NaAuCl₄·2H₂O was dissolved in 1.5 mL of DI water in a 15 mL centrifuge tube, resulting in a transparent yellow solution. Next, 0.0611 g of NaOH was added to this solution producing a dark-orange solution. After being sonicated for 1 h, the solution became transparent yellow. *Solution B* was prepared by dissolving 0.067 g of NH₄Cl, 0.4734 g of Na₂SO₃, and 0.3101 g of Na₂S₂O₃·5H₂O in 25 mL of DI water in a 50 mL centrifuge tube followed by sonication for 1 h. Afterward, solution A, solution B, and 23.5 mL of DI water were combined to reach a total volume of 50 mL and sonicated for 1 h. The resultant colorless solution had 5.75 mM NaAuCl₄·2H₂O₃, 0.075 M Na₂SO₃, 0.025 M Na₂S₂O₃·5H₂O₃, 0.025 M NH₄Cl, and 0.031 M NaOH. This solution was covered with aluminum foil and left undisturbed overnight prior to use.

Preparation of Copper Film. Polycrystalline copper film was deposited onto the reflecting plane of the Si ATR crystal following established methods. 63,64 The surface of the Si prism was polished and treated with Piranha solution as detailed above. The Si prism was then immersed in a 40% NH₄F solution for 90 s at room temperature to afford a hydrophobic hydrogen-terminated surface. Next, the prism surface was immersed in a Cu seeding bath containing 750 μ M CuSO₄ and 0.5 wt % HF for 90 s. After a gentle rinse with DI water, the Si surface was immersed in a freshly prepared Cu deposition bath at 55 °C for 4 min, rinsed with DI water, and dried with flowing N₂. The Cu-coated Si ATR crystal was stored under vacuum before use.

The Cu deposition bath was prepared as follows. First, 10 mL of 0.625 M HCHO solution and 10 mL of 0.05 M CuSO₄ solution were mixed in a 50 mL centrifuge tube, to which another 5 mL of solution containing 100 mM Na₂EDTA and 1.5 mM 2,2-bipyridine was added dropwise. Afterward, NaOH was added to the mixture to raise the pH

to \sim 12. The resulting solution contained 0.25 M HCHO, 0.02 M CuSO₄, 0.3 mM bipyridine, and 20 mM Na₂EDTA.

Preparation of NR Catalyst Film. Typically, $200 \,\mu\text{L}$ of NR solution (5 mg·mL⁻¹ in anhydrous toluene) was drop-cast onto a Si ATR crystal precoated with polycrystalline gold film, which was dried under vacuum at room temperature for 1 h (Figure S28b,c).

Computational Methods. DFT calculations were performed using the Vienna Ab initio Simulation Package (VASP)⁶⁵ with the projector augmented wave pseudopotential^{66,67} and the Revised Perdew–Burke–Ernzerhof (RPBE) exchange-correlation functional.⁶⁸ The Cu(100) supercell was constructed as a (6×4) supercell with three atomic layers. The slab was separated by 12.5 Å of a vacuum layer from the periodic boundaries. We used a $3 \times 3 \times 1$ Monkhorst–Pack k-point mesh and a kinetic energy cutoff for the plane-wave basis of 400 eV. The convergence thresholds for the total energy and force were self-consistent and set to 1×10^{-5} eV and 0.01 eV·Å⁻¹, respectively. The reaction profiles were calculated using 10 intermediate steps between the initial and final steps via the climbingimage nudged elastic band (CI-NEB) method.⁶⁹ All simulations were performed under charge-neutral conditions in vacuum.

To calculate the energetics of the C₁-C₂ coupling step, adsorbed CO (*CO) was used since it is a common C₁ intermediate for generating C_{2+} products during CO_2RR . ^{14,55,70} It has been shown that CO can adsorb to the Cu surface via atop- and bridge-bound modes.⁵⁰ Here, we used atop-bound CO as the C₁ intermediate, whose dominance was revealed by in situ ATR-SEIRAS measurements. The RPBE functional was employed to maximize computational efficiency while correctly predicting the adsorption site and associated activation energy.⁷¹ On the other hand, the dominant C₂ intermediate for C₃ production on the Cu(100) surface is still under debate. 14,17,55 In this work, we examined *HCCH and *HCCH3 as potential C₂ intermediates based on previous studies. 14,55 Our main goal is to understand the effects of Au doping of the Cu(100) surface on the mechanism and energetics of $C_1 - C_2$ coupling during the CO₂RR. We calculated and compared the total Gibbs free energy on both the pristine Cu(100) surface as well as the Cu(100) surface with one of the Cu atoms replaced by one Au atom (Figures S31-S32). Given that Au exhibits low binding affinity toward the *CO intermediate, potential and solvation effects were not considered when evaluating the effect of surface Au atom on the CO2RR. We computed the difference in *CO adsorption energy between Audoped and pristine Cu(100) surfaces as a function of distance from the Au dopant atom (Figure S33). A CO-repulsion zone is present near each Au atom due to its low binding affinity for CO, causing *CO to diffuse to nearby Cu atoms.

ASSOCIATED CONTENT

Supporting Information

The Supporting Information is available free of charge at https://pubs.acs.org/doi/10.1021/jacs.3c11013.

Experimental section; structural characterization of Au/Cu DMA NR catalysts; description of CO₂RR measurement setup and product analysis; additional results of CO₂RR testing; in situ ATR-SEIRAS analysis; and DFT calculations (Figures S1–S33) (Tables S1–S10) (PDF)

AUTHOR INFORMATION

Corresponding Authors

Yuanyue Liu — Texas Materials Institute, The University of Texas at Austin, Austin, Texas 78712, United States; orcid.org/0000-0002-5880-8649; Email: yuanyue.liu@austin.utexas.edu

Xingchen Ye — Department of Chemistry, Indiana University, Bloomington, Indiana 47405, United States; orcid.org/0000-0001-6851-2721; Email: xingye@indiana.edu

Authors

Soojin Jeong — Department of Chemistry, Indiana University, Bloomington, Indiana 47405, United States; ocid.org/0000-0002-5106-216X

Chuanliang Huang – Department of Chemistry, Indiana University, Bloomington, Indiana 47405, United States

Zachary Levell – Texas Materials Institute, The University of Texas at Austin, Austin, Texas 78712, United States

Rebecca X. Skalla – Department of Chemistry, Indiana University, Bloomington, Indiana 47405, United States; orcid.org/0000-0003-0514-2780

Wei Hong – Department of Chemistry, Purdue University, West Lafayette, Indiana 47907, United States; orcid.org/ 0000-0001-7866-9917

Nicole J. Escorcia – Department of Chemistry, Purdue University, West Lafayette, Indiana 47907, United States

Yaroslav Losovyj – Department of Chemistry, Indiana University, Bloomington, Indiana 47405, United States

Baixu Zhu – Department of Chemistry, Indiana University, Bloomington, Indiana 47405, United States

Alex N. Butrum-Griffith – Department of Chemistry, Indiana University, Bloomington, Indiana 47405, United States

Yang Liu – Department of Chemistry, Indiana University, Bloomington, Indiana 47405, United States

Christina W. Li — Department of Chemistry, Purdue University, West Lafayette, Indiana 47907, United States; orcid.org/0000-0002-3538-9955

Danielle Reifsnyder Hickey – Department of Chemistry and Department of Materials Science and Engineering, The Pennsylvania State University, University Park, Pennsylvania 16802, United States; orcid.org/0000-0002-8962-1473

Complete contact information is available at: https://pubs.acs.org/10.1021/jacs.3c11013

Author Contributions

[#]S.J., C.H., and Z.L. contributed equally to this work.

Notes

The authors declare no competing financial interest.

ACKNOWLEDGMENTS

S.J., C.H., R.X.S., B.Z., Y.L., and X.Y. were supported by the U.S. National Science Foundation under award CHE-2239441. C.H. also acknowledges support from the China Scholarship Council and College of Arts and Sciences Dissertation Research Fellowship at Indiana University. Z.L. and Y.L. acknowledge support from the U.S. National Science Foundation under grant numbers CHE-1900039 and EFMA-2029442, ACS PRF (60934-DNI6), and the Welch Foundation (grant no. F-1959-20210327). The DFT calculations used computational resources provided by ACCESS and TACC. W.H., N.J.E., and C.W.L. acknowledge support from the U.S. National Science Foundation under award CHE-2045013. The authors thank Dr. Joshua Wright, Dr. Mark Warren, and Dr. Yujia Ding for their help with XAS experiments. Use of the Advanced Photon Source was supported by the U.S. Department of Energy, Office of Science, Office of Basic Energy Sciences, under contract DE-AC02-06CH11357. MRCAT operations were supported by the Department of Energy and the MRCAT member institutions. D.R.H. acknowledges the Penn State Eberly College of Science, Department of Chemistry, and Materials Research Institute for

generous support through startup funds. The authors acknowledge use of the Penn State Materials Characterization Lab.

REFERENCES

- (1) Li, C. W.; Kanan, M. W. CO₂ Reduction at Low Overpotential on Cu Electrodes Resulting from the Reduction of Thick Cu₂O Films. *J. Am. Chem. Soc.* **2012**, *134*, 7231–7234.
- (2) Kim, D.; Resasco, J.; Yu, Y.; Asiri, A. M.; Yang, P. Synergistic Geometric and Electronic Effects for Electrochemical Reduction of Carbon Dioxide Using Gold-Copper Bimetallic Nanoparticles. *Nat. Commun.* **2014**, *5*, 4948.
- (3) Morales-Guio, C. G.; Cave, E. R.; Nitopi, S. A.; Feaster, J. T.; Wang, L.; Kuhl, K. P.; Jackson, A.; Johnson, N. C.; Abram, D. N.; Hatsukade, T.; Hahn, C.; Jaramillo, T. F. Improved CO₂ Reduction Activity Towards C₂₊ Alcohols on a Tandem Gold on Copper Electrocatalyst. *Nat. Catal.* **2018**, *1*, 764–771.
- (4) Nitopi, S.; Bertheussen, E.; Scott, S. B.; Liu, X.; Engstfeld, A. K.; Horch, S.; Seger, B.; Stephens, I. E. L.; Chan, K.; Hahn, C.; Nørskov, J. K.; Jaramillo, T. F.; Chorkendorff, I. Progress and Perspectives of Electrochemical CO₂ Reduction on Copper in Aqueous Electrolyte. *Chem. Rev.* **2019**, *119*, 7610–7672.
- (5) Verma, S.; Lu, S.; Kenis, P. J. A. Co-Electrolysis of CO₂ and Glycerol as a Pathway to Carbon Chemicals with Improved Technoeconomics due to Low Electricity Consumption. *Nat. Energy* **2019**, *4*, 466–474.
- (6) Shin, H.; Hansen, K. U.; Jiao, F. Techno-Economic Assessment of Low-Temperature Carbon Dioxide Electrolysis. *Nat. Sustain.* **2021**, *4*, 911–919.
- (7) Ren, D.; Wong, N. T.; Handoko, A. D.; Huang, Y.; Yeo, B. S. Mechanistic Insights into the Enhanced Activity and Stability of Agglomerated Cu Nanocrystals for the Electrochemical Reduction of Carbon Dioxide to *n*-Propanol. *J. Phys. Chem. Lett.* **2016**, *7*, 20–24.
- (8) Zhuang, T.-T.; Pang, Y.; Liang, Z.-Q.; Wang, Z.; Li, Y.; Tan, C.-S.; Li, J.; Dinh, C. T.; De Luna, P.; Hsieh, P.-L.; Burdyny, T.; Li, H.-H.; Liu, M.; Wang, Y.; Li, F.; Proppe, A.; Johnston, A.; Nam, D.-H.; Wu, Z.-Y.; Zheng, Y.-R.; Ip, A. H.; Tan, H.; Chen, L.-J.; Yu, S.-H.; Kelley, S. O.; Sinton, D.; Sargent, E. H. Copper Nanocavities Confine Intermediates for Efficient Electrosynthesis of C₃ Alcohol Fuels from Carbon Monoxide. *Nat. Catal.* **2018**, *1*, 946–951.
- (9) Zhuang, T.-T.; Liang, Z.-Q.; Seifitokaldani, A.; Li, Y.; De Luna, P.; Burdyny, T.; Che, F.; Meng, F.; Min, Y.; Quintero-Bermudez, R.; Dinh, C. T.; Pang, Y.; Zhong, M.; Zhang, B.; Li, J.; Chen, P.-N.; Zheng, X.-L.; Liang, H.; Ge, W.-N.; Ye, B.-J.; Sinton, D.; Yu, S.-H.; Sargent, E. H. Steering Post-C—C Coupling Selectivity Enables High Efficiency Electroreduction of Carbon Dioxide to Multi-Carbon Alcohols. *Nat. Catal.* **2018**, *1*, 421–428.
- (10) Li, F.; Li, Y. C.; Wang, Z.; Li, J.; Nam, D.-H.; Lum, Y.; Luo, M.; Wang, X.; Ozden, A.; Hung, S.-F.; Chen, B.; Wang, Y.; Wicks, J.; Xu, Y.; Li, Y.; Gabardo, C. M.; Dinh, C.-T.; Wang, Y.; Zhuang, T.-T.; Sinton, D.; Sargent, E. H. Cooperative CO₂-to-Ethanol Conversion via Enriched Intermediates at Molecule—Metal Catalyst Interfaces. *Nat. Catal.* **2020**, *3*, 75–82.
- (11) Pang, Y.; Li, J.; Wang, Z.; Tan, C.-S.; Hsieh, P.-L.; Zhuang, T.-T.; Liang, Z.-Q.; Zou, C.; Wang, X.; De Luna, P.; Edwards, J. P.; Xu, Y.; Li, F.; Dinh, C.-T.; Zhong, M.; Lou, Y.; Wu, D.; Chen, L.-J.; Sargent, E. H.; Sinton, D. Efficient Electrocatalytic Conversion of Carbon Monoxide to Propanol Using Fragmented Copper. *Nat. Catal.* **2019**, *2*, 251–258.
- (12) Xiao, H.; Cheng, T.; Goddard, W. A. Atomistic Mechanisms Underlying Selectivities in C_1 and C_2 Products from Electrochemical Reduction of CO on Cu(111). *J. Am. Chem. Soc.* **2017**, *139*, 130–136.
- (13) Zheng, Y.; Vasileff, A.; Zhou, X.; Jiao, Y.; Jaroniec, M.; Qiao, S.-Z. Understanding the Roadmap for Electrochemical Reduction of CO₂ to Multi-Carbon Oxygenates and Hydrocarbons on Copper-Based Catalysts. *J. Am. Chem. Soc.* **2019**, *141*, 7646–7659.
- (14) Tang, M. T.; Peng, H.-J.; Stenlid, J. H.; Abild-Pedersen, F. Exploring Trends on Coupling Mechanisms toward C₃ Product Formation in CO₂R. *J. Phys. Chem. C* **2021**, *125*, 26437–26447.

- (15) Jiang, K.; Sandberg, R. B.; Akey, A. J.; Liu, X.; Bell, D. C.; Nørskov, J. K.; Chan, K.; Wang, H. Metal Ion Cycling of Cu Foil for Selective C–C Coupling in Electrochemical CO₂ Reduction. *Nat. Catal.* **2018**, *1*, 111–119.
- (16) Zhong, D.; Zhao, Z.-J.; Zhao, Q.; Cheng, D.; Liu, B.; Zhang, G.; Deng, W.; Dong, H.; Zhang, L.; Li, J.; Li, J.; Gong, J. Coupling of Cu(100) and (110) Facets Promotes Carbon Dioxide Conversion to Hydrocarbons and Alcohols. *Angew. Chem., Int. Ed.* **2021**, *60*, 4879–4885.
- (17) Peng, C.; Luo, G.; Zhang, J.; Chen, M.; Wang, Z.; Sham, T.-K.; Zhang, L.; Li, Y.; Zheng, G. Double Sulfur Vacancies by Lithium Tuning Enhance CO_2 Electroreduction to *n*-Propanol. *Nat. Commun.* **2021**, *12*, 1580.
- (18) Yang, B.; Chen, L.; Xue, S.; Sun, H.; Feng, K.; Chen, Y.; Zhang, X.; Xiao, L.; Qin, Y.; Zhong, J.; Deng, Z.; Jiao, Y.; Peng, Y. Electrocatalytic CO₂ Reduction to Alcohols by Modulating the Molecular Geometry and Cu Coordination in Bicentric Copper Complexes. *Nat. Commun.* **2022**, *13*, 5122.
- (19) Hori, Y. I. Electrochemical CO₂ Reduction on Metal Electrodes. In *Modern Aspects of Electrochemistry*; Vayenas, C. G.; White, R. E.; Gamboa-Aldeco, M. E., Eds.; Springer: New York, NY, 2008; pp 89–189.
- (20) Kuhl, K. P.; Cave, E. R.; Abram, D. N.; Jaramillo, T. F. New Insights into the Electrochemical Reduction of Carbon Dioxide on Metallic Copper Surfaces. *Energy Environ. Sci.* **2012**, *5*, 7050–7059.
- (21) Li, C. W.; Ciston, J.; Kanan, M. W. Electroreduction of Carbon Monoxide to Liquid Fuel on Oxide-Derived Nanocrystalline Copper. *Nature* **2014**, *508*, 504–507.
- (22) Reske, R.; Mistry, H.; Behafarid, F.; Roldan Cuenya, B.; Strasser, P. Particle Size Effects in the Catalytic Electroreduction of CO₂ on Cu Nanoparticles. *J. Am. Chem. Soc.* **2014**, *136*, 6978–6986.
- (23) Grosse, P.; Gao, D.; Scholten, F.; Sinev, I.; Mistry, H.; Roldan Cuenya, B. Dynamic Changes in the Structure, Chemical State and Catalytic Selectivity of Cu Nanocubes During CO₂ Electroreduction: Size and Support Effects. *Angew. Chem., Int. Ed.* **2018**, *57*, 6192–6197.
- (24) Ma, W.; Xie, S.; Liu, T.; Fan, Q.; Ye, J.; Sun, F.; Jiang, Z.; Zhang, Q.; Cheng, J.; Wang, Y. Electrocatalytic Reduction of CO₂ to Ethylene and Ethanol through Hydrogen-Assisted C–C Coupling over Fluorine-Modified Copper. *Nat. Catal.* **2020**, *3*, 478–487.
- (25) Zheng, M.; Wang, P.; Zhi, X.; Yang, K.; Jiao, Y.; Duan, J.; Zheng, Y.; Qiao, S.-Z. Electrocatalytic CO₂-to-C₂₊ with Ampere-Level Current on Heteroatom-Engineered Copper via Tuning *CO Intermediate Coverage. *J. Am. Chem. Soc.* **2022**, *144*, 14936–14944.
- (26) Yang, Y.; Louisia, S.; Yu, S.; Jin, J.; Roh, I.; Chen, C.; Fonseca Guzman, M. V.; Feijóo, J.; Chen, P.-C.; Wang, H.; Pollock, C. J.; Huang, X.; Shao, Y.-T.; Wang, C.; Muller, D. A.; Abruña, H. D.; Yang, P. Operando Studies Reveal Active Cu Nanograins for CO₂ Electroreduction. *Nature* **2023**, *614*, 262–269.
- (27) Calle-Vallejo, F.; Koper, M. T. M. Theoretical Considerations on the Electroreduction of CO to C_2 Species on Cu(100) Electrodes. Angew. Chem., Int. Ed. **2013**, 52, 7282–7285.
- (28) Zaza, L.; Rossi, K.; Buonsanti, R. Well-Defined Copper-Based Nanocatalysts for Selective Electrochemical Reduction of CO₂ to C₂ Products. ACS Energy Lett. **2022**, 7, 1284–1291.
- (29) Clark, E. L.; Resasco, J.; Landers, A.; Lin, J.; Chung, L.-T.; Walton, A.; Hahn, C.; Jaramillo, T. F.; Bell, A. T. Standards and Protocols for Data Acquisition and Reporting for Studies of the Electrochemical Reduction of Carbon Dioxide. *ACS Catal.* **2018**, *8*, 6560–6570.
- (30) Lee, J. D.; Miller, J. B.; Shneidman, A. V.; Sun, L.; Weaver, J. F.; Aizenberg, J.; Biener, J.; Boscoboinik, J. A.; Foucher, A. C.; Frenkel, A. I.; van der Hoeven, J. E. S.; Kozinsky, B.; Marcella, N.; Montemore, M. M.; Ngan, H. T.; O'Connor, C. R.; Owen, C. J.; Stacchiola, D. J.; Stach, E. A.; Madix, R. J.; Sautet, P.; Friend, C. M. Dilute Alloys Based on Au, Ag, or Cu for Efficient Catalysis: From Synthesis to Active Sites. *Chem. Rev.* **2022**, *122*, 8758–8808.
- (31) Hannagan, R. T.; Giannakakis, G.; Flytzani-Stephanopoulos, M.; Sykes, E. C. H. Single-Atom Alloy Catalysis. *Chem. Rev.* **2020**, 120, 12044–12088.

- (32) Greiner, M. T.; Jones, T. E.; Beeg, S.; Zwiener, L.; Scherzer, M.; Girgsdies, F.; Piccinin, S.; Armbrüster, M.; Knop-Gericke, A.; Schlögl, R. Free-Atom-Like *d* States in Single-Atom Alloy Catalysts. *Nat. Chem.* **2018**, *10*, 1008–1015.
- (33) Fu, J.; Zhu, W.; Chen, Y.; Yin, Z.; Li, Y.; Liu, J.; Zhang, H.; Zhu, J.-J.; Sun, S. Bipyridine-Assisted Assembly of Au Nanoparticles on Cu Nanowires to Enhance the Electrochemical Reduction of CO₂. *Angew. Chem., Int. Ed.* **2019**, *58*, 14100–14103.
- (34) Lum, Y.; Ager, J. W. Sequential Catalysis Controls Selectivity in Electrochemical CO₂ Reduction on Cu. *Energy Environ. Sci.* **2018**, *11*, 2935–2944.
- (35) Ren, D.; Ang, B. S.-H.; Yeo, B. S. Tuning the Selectivity of Carbon Dioxide Electroreduction toward Ethanol on Oxide-Derived Cu_xZn Catalysts. *ACS Catal.* **2016**, *6*, 8239–8247.
- (36) Louisia, S.; Kim, D.; Li, Y.; Gao, M.; Yu, S.; Roh, I.; Yang, P. The Presence and Role of the Intermediary CO Reservoir in Heterogeneous Electroreduction of CO₂. *Proc. Natl. Acad. Sci. U.S.A.* **2022**, *119*, e2201922119.
- (37) Zheng, T.; Liu, C.; Guo, C.; Zhang, M.; Li, X.; Jiang, Q.; Xue, W.; Li, H.; Li, A.; Pao, C.-W.; Xiao, J.; Xia, C.; Zeng, J. Copper-Catalysed Exclusive CO₂ to Pure Formic Acid Conversion via Single-Atom Alloying. *Nat. Nanotechnol.* **2021**, *16*, 1386–1393.
- (38) Liu, K.; Ma, M.; Wu, L.; Valenti, M.; Cardenas-Morcoso, D.; Hofmann, J. P.; Bisquert, J.; Gimenez, S.; Smith, W. A. Electronic Effects Determine the Selectivity of Planar Au—Cu Bimetallic Thin Films for Electrochemical CO₂ Reduction. *ACS Appl. Mater. Interfaces* **2019**, *11*, 16546–16555.
- (39) Jeong, S.; Liu, Y.; Zhong, Y.; Zhan, X.; Li, Y.; Wang, Y.; Cha, P. M.; Chen, J.; Ye, X. Heterometallic Seed-Mediated Growth of Monodisperse Colloidal Copper Nanorods with Widely Tunable Plasmonic Resonances. *Nano Lett.* **2020**, *20*, 7263–7271.
- (40) Kuhn, M.; Sham, T. K. Charge Redistribution and Electronic Behavior in a Series of Au-Cu Alloys. *Phys. Rev. B* **1994**, 49, 1647–1661.
- (41) Liu, X.; Ao, C.; Shen, X.; Wang, L.; Wang, S.; Cao, L.; Zhang, W.; Dong, J.; Bao, J.; Ding, T.; Zhang, L.; Yao, T. Dynamic Surface Reconstruction of Single-Atom Bimetallic Alloy under Operando Electrochemical Conditions. *Nano Lett.* **2020**, *20*, 8319–8325.
- (42) Wang, Y.; Cao, L.; Libretto, N. J.; Li, X.; Li, C.; Wan, Y.; He, C.; Lee, J.; Gregg, J.; Zong, H.; Su, D.; Miller, J. T.; Mueller, T.; Wang, C. Ensemble Effect in Bimetallic Electrocatalysts for CO₂ Reduction. *J. Am. Chem. Soc.* **2019**, *141*, 16635–16642.
- (43) Wrasman, C. J.; Boubnov, A.; Riscoe, A. R.; Hoffman, A. S.; Bare, S. R.; Cargnello, M. Synthesis of Colloidal Pd/Au Dilute Alloy Nanocrystals and Their Potential for Selective Catalytic Oxidations. *J. Am. Chem. Soc.* **2018**, *140*, 12930–12939.
- (44) Verma, S.; Hamasaki, Y.; Kim, C.; Huang, W.; Lu, S.; Jhong, H.-R. M.; Gewirth, A. A.; Fujigaya, T.; Nakashima, N.; Kenis, P. J. A. Insights into the Low Overpotential Electroreduction of CO₂ to CO on a Supported Gold Catalyst in an Alkaline Flow Electrolyzer. ACS Energy Lett. **2018**, *3*, 193–198.
- (45) Ma, S.; Sadakiyo, M.; Luo, R.; Heima, M.; Yamauchi, M.; Kenis, P. J. A. One-Step Electrosynthesis of Ethylene and Ethanol from CO₂ in an Alkaline Electrolyzer. *J. Power Sources* **2016**, 301, 219–228.
- (46) Lv, J.-J.; Jouny, M.; Luc, W.; Zhu, W.; Zhu, J.-J.; Jiao, F. A Highly Porous Copper Electrocatalyst for Carbon Dioxide Reduction. *Adv. Mater.* **2018**, *30*, 1803111.
- (47) Kibria, M. G.; Dinh, C.-T.; Seifitokaldani, A.; De Luna, P.; Burdyny, T.; Quintero-Bermudez, R.; Ross, M. B.; Bushuyev, O. S.; García de Arquer, F. P.; Yang, P.; Sinton, D.; Sargent, E. H. A Surface Reconstruction Route to High Productivity and Selectivity in CO₂ Electroreduction toward C₂₊ Hydrocarbons. *Adv. Mater.* **2018**, *30*, 1804867.
- (48) Romero Cuellar, N. S.; Wiesner-Fleischer, K.; Fleischer, M.; Rucki, A.; Hinrichsen, O. Advantages of CO over CO₂ as Reactant for Electrochemical Reduction to Ethylene, Ethanol and *n*-Propanol on Gas Diffusion Electrodes at High Current Densities. *Electrochim. Acta* **2019**, 307, 164–175.

- (49) Gunathunge, C. M.; Li, X.; Li, J.; Hicks, R. P.; Ovalle, V. J.; Waegele, M. M. Spectroscopic Observation of Reversible Surface Reconstruction of Copper Electrodes under CO₂ Reduction. *J. Phys. Chem. C* **2017**, *121*, 12337–12344.
- (50) Gunathunge, C. M.; Ovalle, V. J.; Li, Y.; Janik, M. J.; Waegele, M. M. Existence of an Electrochemically Inert CO Population on Cu Electrodes in Alkaline pH. ACS Catal. 2018, 8, 7507–7516.
- (51) Malkani, A. S.; Li, J.; Oliveira, N. J.; He, M.; Chang, X.; Xu, B.; Lu, Q. Understanding the Electric and Nonelectric Field Components of the Cation Effect on the Electrochemical CO Reduction Reaction. *Sci. Adv.* **2020**, *6*, eabd2569.
- (52) Malkani, A. S.; Dunwell, M.; Xu, B. Operando Spectroscopic Investigations of Copper and Oxide-Derived Copper Catalysts for Electrochemical CO Reduction. *ACS Catal.* **2019**, *9*, 474–478.
- (53) Bagus, P. S.; Pacchioni, G. Electric Field Effects on the Surface—Adsorbate Interaction: Cluster Model Studies. *Electrochim. Acta* 1991, 36, 1669–1675.
- (54) Gunathunge, C. M.; Li, J.; Li, X.; Hong, J. J.; Waegele, M. M. Revealing the Predominant Surface Facets of Rough Cu Electrodes under Electrochemical Conditions. *ACS Catal.* **2020**, *10*, 6908–6923.
- (55) Hori, Y.; Takahashi, R.; Yoshinami, Y.; Murata, A. Electrochemical Reduction of CO at a Copper Electrode. *J. Phys. Chem. B* **1997**, *101*, 7075–7081.
- (56) Zhang, H.; Zhang, Y.; Li, Y.; Ahn, S.; Palmore, G. T. R.; Fu, J.; Peterson, A. A.; Sun, S. Cu Nanowire-Catalyzed Electrochemical Reduction of CO or CO₂. *Nanoscale* **2019**, *11*, 12075–12079.
- (57) Loiudice, A.; Lobaccaro, P.; Kamali, E. A.; Thao, T.; Huang, B. H.; Ager, J. W.; Buonsanti, R. Tailoring Copper Nanocrystals Towards C₂ Products in Electrochemical CO₂ Reduction. *Angew. Chem., Int. Ed.* **2016**, *55*, 5789–5792.
- (58) Blume, R.; Rosenthal, D.; Tessonnier, J.-P.; Li, H.; Knop-Gericke, A.; Schlögl, R. Characterizing Graphitic Carbon with X-Ray Photoelectron Spectroscopy: A Step-by-Step Approach. *ChemCatChem* **2015**, *7*, 2871–2881.
- (59) Ravel, B.; Newville, M. Athena, Artemis, Hephaestus: Data Analysis for X-Ray Absorption Spectroscopy Using IFEFFIT. *J. Synchrotron Radiat.* **2005**, *12*, 537–541.
- (60) Huang, J.; Mensi, M.; Oveisi, E.; Mantella, V.; Buonsanti, R. Structural Sensitivities in Bimetallic Catalysts for Electrochemical CO₂ Reduction Revealed by Ag-Cu Nanodimers. *J. Am. Chem. Soc.* **2019**, *141*, 2490–2499.
- (61) Luc, W.; Fu, X.; Shi, J.; Lv, J.-J.; Jouny, M.; Ko, B. H.; Xu, Y.; Tu, Q.; Hu, X.; Wu, J.; Yue, Q.; Liu, Y.; Jiao, F.; Kang, Y. Two-Dimensional Copper Nanosheets for Electrochemical Reduction of Carbon Monoxide to Acetate. *Nat. Catal.* **2019**, *2*, 423–430.
- (62) Miyake, H.; Ye, S.; Osawa, M. Electroless Deposition of Gold Thin Films on Silicon for Surface-Enhanced Infrared Spectroelectrochemistry. *Electrochem. Commun.* **2002**, *4*, 973–977.
- (63) Wang, H.-F.; Yan, Y.-G.; Huo, S.-J.; Cai, W.-B.; Xu, Q.-J.; Osawa, M. Seeded Growth Fabrication of Cu-on-Si Electrodes for *in situ* ATR-SEIRAS Applications. *Electrochim. Acta* **2007**, *52*, 5950–5957.
- (64) Wuttig, A.; Liu, C.; Peng, Q.; Yaguchi, M.; Hendon, C. H.; Motobayashi, K.; Ye, S.; Osawa, M.; Surendranath, Y. Tracking a Common Surface-Bound Intermediate During CO₂-to-Fuels Catalysis. *ACS Cent. Sci.* **2016**, *2*, 522–528.
- (65) Kresse, G.; Furthmüller, J. Efficiency of Ab-Initio Total Energy Calculations for Metals and Semiconductors Using a Plane-Wave Basis Set. *Comput. Mater. Sci.* **1996**, *6*, 15–50.
- (66) Blöchl, P. E. Projector Augmented-Wave Method. *Phys. Rev. B* **1994**, *50*, 17953–17979.
- (67) Kresse, G.; Furthmüller, J. Efficient Iterative Schemes for Ab Initio Total-Energy Calculations Using a Plane-Wave Basis Set. *Phys. Rev. B* **1996**, *54*, 11169–11186.
- (68) Hammer, B.; Hansen, L. B.; Nørskov, J. K. Improved Adsorption Energetics within Density-Functional Theory Using Revised Perdew-Burke-Ernzerhof Functionals. *Phys. Rev. B* **1999**, *59*, 7413–7421.

- (69) Henkelman, G.; Uberuaga, B. P.; Jónsson, H. A Climbing Image Nudged Elastic Band Method for Finding Saddle Points and Minimum Energy Paths. *J. Chem. Phys.* **2000**, *113*, 9901–9904.
- (70) Cheng, T.; Xiao, H.; Goddard, W. A. Full Atomistic Reaction Mechanism with Kinetics for CO Reduction on Cu(100) from Ab Initio Molecular Dynamics Free-Energy Calculations at 298 K. *Proc. Natl. Acad. Sci. U. S. A.* **2017**, *114*, 1795–1800.
- (71) Wei, Z.; Göltl, F.; Sautet, P. Diffusion Barriers for Carbon Monoxide on the Cu(001) Surface Using Many-Body Perturbation Theory and Various Density Functionals. *J. Chem. Theory Comput.* **2021**, *17*, 7862–7872.